IEICE TRANSACTIONS

on Fundamentals of Electronics, Communications and Computer Sciences

This advance publication article will be replaced by the finalized version after proofreading.

PAPER

Principle Analysis for the Possibility of Scattered X-ray to Improve Computed Tomography Reconstruction

Naohiro TODA[†a)], *Member and* **Tetsuya NAKAGAMI**[††b)], *Nonmember*

SUMMARY If scattered X-rays carry information that is independent of that is carried by primary X-rays, the accuracy of attenuation coefficients estimated using both primary and scattered X-rays is expected to be better than that estimated using only primary X-rays. However, because scattered X-rays cannot be easily introduced into conventional X-ray computed tomography (CT), the issue has gained scant attention. This study demonstrates theoretically that the measurement of scattered X-rays improves the accuracy of reconstruction in CT, even in a photoelectric absorption scenario. Here, the CT geometry was simplified for a system that targeted a homogeneous thin cylinder, retaining the necessary configuration. Furthermore, we constructed a mathematical model termed the π-junction model. This model is an extension of the T-junction model used in one of our previous studies. It addresses the photoelectric effect, which was not considered in the T-junction model. The variance in the estimation of the attenuation coefficients of this model from the measurements of both primary and scattered photons was evaluated as the Cramer-Rao lower bound. Both the theory and numerical experiments using Monte Carlo simulation showed that the accuracy of estimating the attenuation coefficient could be improved by measuring the scattered X-rays together with the primary X-rays, even in the presence of photoelectric absorption. This result provides a basis for the superiority of using scattered X-rays.

key words: X-ray CT, scattered X-ray, photoelectric absorption, accuracy, Cramer–Rao lower-bound, Monte Carlo simulation

1. Introduction

X-ray computed tomography (CT) is a technique that provides images of the inside of a body rapidly, which is indispensable in modern medical care [1]. With recent advances in diagnostic support technology [2], its performance can be demonstrated in terms of high speed, high definition, and low radiation exposure [3].

In CT, the density of reconstructed images corresponds to the linear attenuation coefficient of the object, which is typically estimated by measuring the primary X-rays, that is, photons that pass directly through the object. X-rays that interact with an object and which do not pass directly are absorbed by the photoelectric effect or are scattered, changing their traveling direction and energy.

The scattered X-rays cannot be differentiated from the primary X-rays by a sensor and, if not eliminated, can lead to artefacts in the reconstructed image [1], [4], [5]. Many scatter-correction methods have been proposed to prevent the occurrence of artefacts. An anti-scatter grid (or post-patient collimator) [1], [6] and beam-stop arrays [7]–[9] use hardware that controls the X-ray beam. The two types of scatter-correction approaches that are based on software are a kernel-based method [10], [11] and a technique based on Monte Carlo simulation [11]–[14]. These scatter-correction strategies involve subtracting the scatter estimations from the original projections, and hence, the scattered X-rays are ignored. Ordinary CT eliminates scattered X-rays because current reconstruction algorithms assume that projection data consist of only primary X-rays, due to the present limited computer capabilities.

As X-rays are scattered by an object, the scattered X-rays contain information about the object. From this perspective, several studies have investigated tomographic imaging using scattered X-rays [15]–[22]. Particularly, Norton's modality [18] and its improvements [19]–[22] involve new concepts. However, this is considered a different modality from conventional X-ray CT. If scattered X-rays contain information that is independent of that provided by primary X-rays, the accuracy of attenuation coefficients estimated using both primary and scattered X-rays are expected to be better than that estimated using only primary X-rays. However, since scattered X-rays cannot be easily introduced into conventional X-ray CT, this issue has gained scant attention.

Owing to the recent enhanced computational capability, two strategies can be used to address this issue. The first is based on the total simulation of the CT geometric structure and the interactions between X-rays and substances [23]–[25]. In this method, an image is reconstructed by converging virtually generated projection data in a computer to the measured projection data using an iterative optimization algorithm. We refer to these methods as simulated-projection-based methods. The introduction of scattering phenomena, including multiple scattering, into a simulation model eliminated the restriction of only primary X-rays being used. Therefore, the simulated projection-based method can estimate the attenuation coefficient using scattered and primary X-rays. In this connection, we conducted a numerical experiment on the simulated projection-based method using Monte Carlo simulation for a small-scale target object and investigated the possibility of improving the reconstruction accuracy by using scattered X-rays [26].

The second method used machine learning. Advances in computers have increased the scale of artificial neural

[†]School of Information Science and Technology, Aichi Prefectural University, Ibaragabasama 1522-3, Kumabari, Nagakute-shi, Aichi-ken, 480-1198 Japan

[††]DENSO CREATE INC. Technical Resources Department, Hirokoji Daiichiseimei Bldg, Sakae, Naka-ku, Nagoya-shi, Aichi-ken, 460-0008, Japan

a) E-mail: toda@ist.aichi-pu.ac.jp
b) E-mail: dmroas.gqouni.ftloy1024@gmail.com

networks (ANNs), enabling them to perform various recognition tasks and generate high-quality images and sentences [27]. Their excellent performances have also been utilized in the medical field [2]. In CT reconstruction, the projection data of many objects are obtained using phantoms or are created by simulations, and networks that receive these data as input are trained to output tomographic images [28], [29]. Because scattered X-rays should also reflect differences in the internal structure of an object, a reconstruction method can be realized using scattered X-rays by learning to output tomographic images. We previously reported a numerical example to show that the reconstruction accuracy is better for a small object using scattered X-rays than using only primary X-rays [30].

These numerical examples raise expectations regarding the use of scattered X-rays on a practical scale. However, since this is a novel idea, its theoretical basis has not been sufficiently established. We simplified the CT geometry, assumed a homogeneous thin cylinder as an object, developed a T-junction mathematical model, and analytically demonstrated the superiority of using scattered X-rays [31]. However, photon annihilation due to photoelectric absorption was not considered in the analysis.

In this study, we develop a model that has π-shaped branch paths. Termed a π-junction model, it includes photoelectric absorption by extending the T-junction model, and provides a theoretical basis for the superiority of scattered X-ray measurements. Specifically, the thin cylinder is divided into several segments, in which a detector is installed to detect the segment in which the light is scattered. Each segment corresponds to a π-junction. The probability of scattering and the probability of photoelectric absorption in each segment are set, where it is assumed that these are estimated from the observed number of direct photons and scattered photons. Under these settings, it is theoretically shown that, even if photoelectric absorption is present and the number of scattered photons measured is reduced, the estimation accuracy is improved by measuring scattered radiation in addition to direct radiation as compared to the case where only the direct radiation is considered. Furthermore, this theory is validated by conducting Monte Carlo numerical simulations using maximum likelihood estimation.

2. Simplification of CT geometry

For theoretical analysis, the CT geometry was simplified following the method proposed in [31]. For simplification, we set the following two conditions:

C-1 The estimation accuracy of the attenuation coefficient should be compared for the case of measuring the primary X-ray photons only and the case of measuring both primary and scattered X-ray photons.

C-2 The accuracy should have a variable indicating the incident X-ray photon number.

Condition C-1 describes this purpose. Condition C-2 shows the relationship between the estimation accuracy
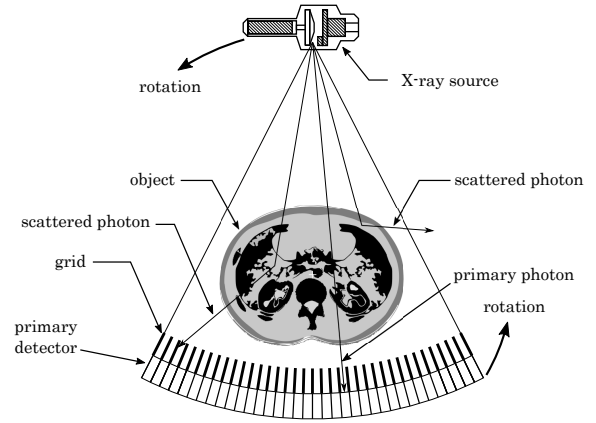

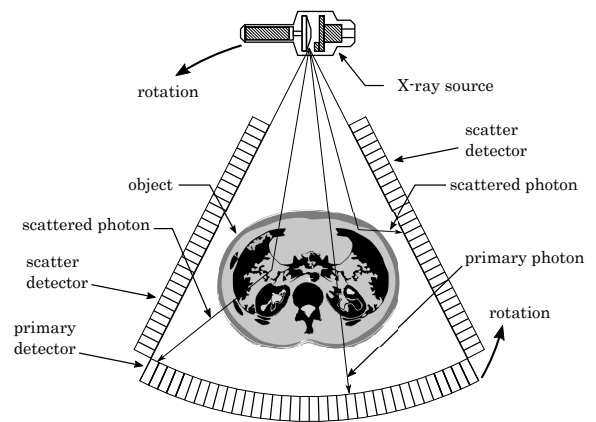**Fig. 1**　Conventional CT geometry

Fig. 2　CT utilizing scattered X-rays

of the attenuation coefficient and the X-ray dose. If these conditions are satisfied, the simplest possible geometry is preferred. Hereinafter, the term scattered X-ray photon is referred to as scattered photon simply through the theory construction process.

As shown in Fig. 1, in a conventional CT, cone-beam X-rays are irradiated and the primary photons that pass through an object are measured using a detector array. Scattered photons are blocked using a grid installed in front of the detector.

By contrast, our future CT system that will use scattered photons will be similar to that shown in Fig. 2. The scattered photons reached the detector since the grid was removed. To capture side and back scatters, it was assumed that dedicated detectors (referred to as scatter detectors) were installed around the object. However, such a CT geometry is extremely complicated for theoretical derivation.

We simplified the geometry by reducing the number of elements comprising the object to one. The target object was a thin cylinder of a homogeneous material, as shown in Fig. 3. The cylinder was exposed to a pencil beam X-rays.

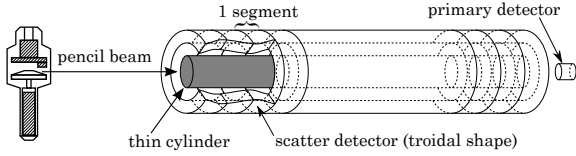Primary photons were measured using a cylindrical de-

TODA and NAKAGAMI: PRINCIPLE ANALYSIS FOR THE POSSIBILITY OF SCATTERED X-RAY TO IMPROVE COMPUTED TOMOGRAPHY RECONSTRUCTION

3

Fig. 3 Simplified CT geometry

(a) T-junction model   (b) π-junction model

Fig. 4 T- and π-junction model

tector (referred to as the primary detector), as shown in Fig. 3. Because the scattered photons radiated around the cylinder isotropically, we used several scatter detectors with toroidal structures for measurement. A set consisting of one scatter detector and a thin cylinder corresponding to its length is defined as one segment. Both the scatter and primary detectors were assumed to count photons without any loss. Photons were assumed to disappear instantaneously when counted by the detectors. This geometry is referred to as a homogeneous thin cylinder.

3. π-junction model

For theoretical consideration, the homogeneous thin cylinder was further abstracted and its mathematical model was developed. In our previous study [31], we used the T-junction model shown in Fig. 4(a) as a model of one segment of the homogeneous thin cylinder.

Let $\mathbb{N}$ be the set of non-negative integers, that is, $\mathbb{N} = \{0, 1, 2, \cdots\}$ and $\mathbb{R}$ be the set of real numbers. We define a finite set $\mathbb{Z}_n$, $(n \in \mathbb{N})$ and its k-times direct product $\mathbb{Z}_n^k$, $(k \in \mathbb{N}, 1 \le k)$ as follows:

$$\mathbb{Z}_n = \{x \in \mathbb{N} \mid x \le n\}, \tag{1}$$

$$\mathbb{Z}_n^k = \underbrace{\mathbb{Z}_n \times \mathbb{Z}_n \times \cdots \times \mathbb{Z}_n}_{k \text{ times}}. \tag{2}$$

In the T-junction model, a photon incident on the left hand end passes through the model and exits from the right hand end with a probability p $(p \in \mathbb{R}, 0 < p \le 1)$. The distance d $(d \in \mathbb{R}, 0 \le d)$ cm travelled by this photon corresponds to the length d of one segment of the thin cylinder. This photon corresponds to the primary photon. Assume that, when n photons are incident, the number of primary photons is x, $(x \in \mathbb{Z}_n)$. Using the attenuation coefficient μ $(\mu \in \mathbb{R}, 0 < \mu)$ and distance d, the probability p can be expressed as $p = \exp(-\mu d)$. However, a photon interacts with matter with a probability of $1 - p$ and changes its traveling direction (indicated by the downward arrow in the figure), which is the scattered photon. This interaction is limited to scattering in the T-junction model.

The mathematical model of a homogeneous thin cylinder formed by connecting k T-junction models in a cascaded manner is termed the k-chained T-junction model. The number of photons input into the k-chained T-junction model is denoted as n, and the number of scattered photons is denoted as y_ℓ $(y_\ell \in \mathbb{Z}_n, 1 \le \ell \le k)$. By analyzing the statistical properties of the k-chained T-junction model, we showed
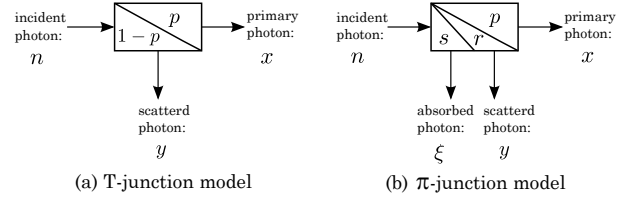
that accuracy of estimation of the attenuation coefficient improves with increasing number of scatter detectors.

However, we would like to build a basis by drawing closer the theoretical conditions to the actual conditions from the ideal conditions. In this study, photoelectric absorption, which was ignored in the T-junction model, was included, and a new model was introduced, as shown in Fig. 4(b). This model, termed the π-junction model has a π-shaped branch path. One branch added to the T-junction model corresponds to photoelectric absorption. As in the T-junction model, an incident photon passes through as a primary photon with probability p. In the π-junction model, the attenuation coefficient μ is composed of the scattering component μ_s $(\mu_s \in \mathbb{R}, 0 \le \mu_s \le \mu)$ and the photoelectric absorption component μ_a $(\mu_a \in \mathbb{R}, 0 \le \mu_a \le \mu)$, which can be expressed as, [32]

$$\mu = \mu_s + \mu_a. \tag{3}$$

From (3), the scattering probability q for the interaction can be expressed as

$$q = \frac{\mu_s}{\mu}. \tag{4}$$

Hereafter, μ_s is termed the scattering coefficient. The probability r that an incident photon scatters at the π-junction is obtained by multiplying the interaction probability $1 - p$ by q,
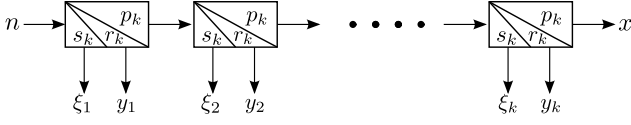
$$r = (1 - p)q. \tag{5}$$

In addition, among the interacting photons, those that are not scattered are photoelectrically absorbed; therefore, the probability s of the incident photons being photoelectrically absorbed is

$$s = (1 - p)(1 - q). \tag{6}$$

Assigning ξ, $(\xi \in \mathbb{Z}_n)$ to the number of photoelectrically absorbed photons, x, y, ξ in the π-junction model follows a multinomial (trinomial) distribution, whose joint probability function $M(x, y, \xi)$ is expressed as,

$$M(x, y, \xi) = \begin{cases} \dfrac{n!}{x!y!\xi!} p^x r^y s^\xi, & (x, y, \xi) \in \mathbb{S}_{M_1}, \\ 0, & (x, y, \xi) \in \mathbb{S}_{M_1}^C, \end{cases} \tag{7}$$

where $\mathbb{S}_{M_1} = \{(x, y, \xi) \in \mathbb{Z}_n^3 \mid x + y + \xi = n\}$ is the support set and its complementary set is $\mathbb{S}_{M_1}^C = \mathbb{Z}_n^3 \setminus \mathbb{S}_{M_1}$. In the π-junction model, only x and y can be measured by detectors,

$n \longrightarrow$ [s_k p_k r_k] $\longrightarrow$ [s_k p_k r_k] $\longrightarrow$ $\bullet \bullet \bullet \bullet \bullet$ $\longrightarrow$ [s_k p_k r_k] $\longrightarrow x$

ξ_1 y_1 $\quad$ ξ_2 y_2 $\quad\quad$ ξ_k y_k

Fig. 5 k-chained π-junction model

whereas the number of absorbed photons ξ is not measured. By eliminating ξ from the above equation using the relationship $\xi = n - x - y$, the probability function $f(x, y \mid \mu, \mu_s)$ can be expressed as

$$f(x, y \mid \mu, \mu_s) = \begin{cases} \dfrac{n!}{x! y! (n - x - y)!} p^x r^y s^{n-x-y}, & (x, y) \in \mathbb{S}_{f_1}, \\ 0, & (x, y) \in \mathbb{S}_{f_1}^C, \end{cases} \quad (8)$$

where $\mathbb{S}_{f_1} = \{(x, y) \in \mathbb{Z}_n^2 \mid 0 \le x + y \le n\}$, $\mathbb{S}_{f_1}^C = \mathbb{Z}_n^2 \setminus \mathbb{S}_{f_1}$.

4. k-chained π-junction model

As shown in Fig. 5, a k-times $(k \in \mathbb{N}, 1 \le k)$ cascade-connected π-junction model is termed a k-chained π-junction model and is used to analyze a homogeneous thin cylinder of length L cm. The π-junction of this model is termed an element. Each element corresponds to one segment of the homogeneous thin cylinder with a length L/k cm and surrounding scatter detector. The probability that a photon passes through each element changes with the total number k of scatter detectors (i.e., the total number of elements), which can be written as,

$$p_k = \exp\left(-\mu \frac{L}{k}\right). \quad (9)$$

However, this probability is constant and independent of the number ℓ ($\ell \in \mathbb{N}, 1 \le \ell \le k$) of elements. Therefore, the probability P_{prim} that a photon passes through all elements without interacting and is output as a primary photon is p_k to a power of k; that is,

$$P_{prim} = (p_k)^k = \left(\exp\left(-\mu \frac{L}{k}\right)\right)^k = \exp\left(-\mu L\right). \quad (10)$$

The probability of scattering in each element also does not depend on the number of elements ℓ but only on k and is obtained by substituting p_k for p in (5) as,

$$r_k = (1 - p_k)q. \quad (11)$$

The probability $P_{sc}(\ell)$ that a photon incident on the k-chained π-junction model is scattered at the ℓ-th element is obtained as a product of r_k and the probability of passing through $\ell - 1$ elements,

$$P_{sc}(\ell) = (p_k)^{\ell-1} r_k . \quad (12)$$

Similarly, the probability of photoelectric absorption in each element s_k is obtained by substituting p_k for p in (6):

$$s_k = (1 - p_k)(1 - q). \quad (13)$$

The probability of photoelectric absorption $P_{ab}(\ell)$ at the ℓ-th element is also obtained as a product of the probability of passing through $\ell - 1$ elements and s_k as

$$P_{ab}(\ell) = (p_k)^{\ell-1} s_k . \quad (14)$$

Although the number of photons ξ_ℓ photoelectrically absorbed by each element cannot be measured, their sum

$$\xi = \sum_{\ell=1}^{k} \xi_\ell \quad (15)$$

can be calculated from the measurable number of primary photons x, scattered photons y_ℓ, and the number of incident photons n, as

$$\xi = n - x - \sum_{\ell=1}^{k} y_\ell . \quad (16)$$

The probability $P_{ab_{all}}$ of the total photoelectric absorption is given by the sum of the probabilities of each ξ_ℓ

$$\begin{aligned} P_{ab_{all}} &= \sum_{\ell=1}^{k} P_{ab}(\ell) \\ &= (1 - p_k)\left(1 - \frac{\mu_s}{\mu}\right) \sum_{\ell=1}^{k} (p_k)^{\ell-1} \\ &= (1 - p_k)\left(1 - \frac{\mu_s}{\mu}\right) \frac{1 - p_k^k}{1 - p_k} \\ &= \left(1 - \frac{\mu_s}{\mu}\right)(1 - \exp(-\mu L)) . \end{aligned} \quad (17)$$

Thus, the stochastic structure of the k-chained π-junction model is a multinomial distribution with respect to the number of primary, scattered, and photoelectrically absorbed photons. In other words, let ${}^k\boldsymbol{y} = (y_1, y_2, \cdots, y_k) \in \mathbb{Z}_n^k$, where the support set $\mathbb{S}_{M_k}$ and its complement set $\mathbb{S}_{M_k}^C$ are

$$\mathbb{S}_{M_k} = \left\{ (x, {}^k\boldsymbol{y}, \xi) \in \mathbb{Z}_n^{k+2} \,\middle|\, x + \sum_{\ell=1}^{k} y_\ell + \xi = n \right\}, \quad (18)$$

$$\mathbb{S}_{M_k}^C = \mathbb{Z}_n^{k+2} \setminus \mathbb{S}_{M_k}. \quad (19)$$

The probability function $M(x, {}^k\boldsymbol{y}, \xi)$ is given by the probabilities of each variable as,

$$M(x, {}^k\boldsymbol{y}, \xi) = \begin{cases} \dfrac{n!}{x! \displaystyle\prod_{\ell=1}^{k} (y_i!) \, \xi!} P_{prim}^x \displaystyle\prod_{\ell=1}^{k} P_{sc}^{y_\ell}(\ell) P_{ab_{all}}^{\xi}, \\ \qquad\qquad\qquad (x, {}^k\boldsymbol{y}, z) \in \mathbb{S}_{M_k}, \\ 0, \qquad\qquad (x, {}^k\boldsymbol{y}, z) \in \mathbb{S}_{M_k}^C. \end{cases} \quad (20)$$

Although, as aforementioned, ξ cannot be measured, by substituting (16) into (20), the probability function $f_k(x, {}^k\boldsymbol{y} \mid$

TODA and NAKAGAMI: PRINCIPLE ANALYSIS FOR THE POSSIBILITY OF SCATTERED X-RAY TO IMPROVE COMPUTED TOMOGRAPHY RECONSTRUCTION

5

μ_s, μ) with measurable variables can be obtained as

$$f_k(x, {}^k\boldsymbol{y} \mid \mu, \mu_s) =$$
$$\begin{cases} M(x, {}^k\boldsymbol{y}, z)\big|_{z=n-x-\sum_{\ell=1}^k y_\ell}, & (x, {}^k\boldsymbol{y}) \in \mathbb{S}_{f_k}, \\ 0, & (x, {}^k\boldsymbol{y}) \in \mathbb{S}_{f_k}^C, \end{cases} \quad (21)$$

where

$$\mathbb{S}_{f_k} = \left\{ (x, {}^k\boldsymbol{y}) \in \mathbb{Z}_n^{k+1} \,\middle|\, 0 \le x + \sum_{\ell=1}^k y_\ell \le n \right\}, \quad (22)$$

$$\mathbb{S}_{f_k}^C = \mathbb{Z}_n^{k+1} \setminus \mathbb{S}_{f_k}. \quad (23)$$

Thus, the following expression is obtained:

$$f_k(x, {}^k\boldsymbol{y} \mid \mu, \mu_s) =$$
$$\begin{cases} \dfrac{n!}{x! \prod_{\ell=1}^k y_\ell! \left(n - x - \sum_{\ell=1}^k y_\ell\right)!} (\exp(-\mu L))^x \\ \quad \cdot \prod_{\ell=1}^k \left\{ \left(\left(\exp\left(-\mu\dfrac{L}{k}\right)\right)^{\ell-1} \left(1 - \exp\left(-\mu\dfrac{L}{k}\right)\right) \dfrac{\mu_s}{\mu}\right\}^{y_\ell} \\ \quad \cdot \left\{\left(1 - \dfrac{\mu_s}{\mu}\right)(1 - \exp(-\mu L))\right\}^{n-x-\sum_{\ell=1}^k y_\ell}, \\ \hspace{8em} (x, {}^k\boldsymbol{y}) \in \mathbb{S}_{f_k}, \\ 0, \hspace{6em} (x, {}^k\boldsymbol{y}) \in \mathbb{S}_{f_k}^C. \end{cases} \quad (24)$$

For primary photon-only measurements, the stochastic structure is a binomial distribution of the number of primary photons x and the number of photons $\eta = n - x$ that interact with the material of the object. Because the probability of passing through a thin cylinder of length L is P_{prim} given by (10), the probability of being scattered or absorbed at some element is $1 - P_{prim}$. Thus, the number of primary photons x and the number of other photons η follow a binomial distribution,

$$B(x) = \begin{cases} \dfrac{n!}{x!\eta!} P_{prim}^x \left(1 - P_{prim}\right)^\eta, & (x, \eta) \in \mathbb{S}_B, \\ 0, & (x, \eta) \in \mathbb{S}_B^C \end{cases} \quad (25)$$

whrere, $\mathbb{S}_B = \{(x, \eta) \in \mathbb{Z}_n^2 \mid x + \eta = n\}$, and $\mathbb{S}_B^C = \mathbb{Z}_n^2 \setminus \mathbb{S}_B$. Therefore, the probability function $f_{prim}(x \mid \mu)$ with only the primary photon number x is obtained by substituting $\eta = n - x$ into (25) as follows:

$$\begin{aligned} f_{prim}(x \mid \mu) &= \frac{n!}{x!(n-x)!} P_{prim}^x \left(1 - P_{prim}\right)^{n-x} \\ &= \frac{n!}{x!(n-x)!} (\exp(-\mu L))^x (1 - \exp(-\mu L))^{n-x}, \\ &\hspace{12em} x \in \mathbb{Z}_n. \end{aligned} \quad (26)$$

It is clear that f_{prim} does not depend on the parameter μ_s; that is, the scattering coefficient cannot be determined by measuring only the primary photon number.

5. Accuracy Criterion

Herein, we derive a criterion for evaluating the estimation accuracy of the unknown parameters μ and μ_s. Because the arrival of photons at a detector is a stochastic phenomenon, the estimated attenuation coefficients fluctuate randomly. When the estimated parameters are unbiased, accuracy is generally evaluated using a variance–covariance matrix. If the estimation method is considered to provide satisfactory efficiency, the variances will never be less than the Cramer–Rao lower bound [33]. A noteworthy feature of this bound is that if the stochastic structures (i.e., probability functions) of the methods differ, their accuracies can be compared analytically without explicitly constructing an estimator. Fortunately, the stochastic structure differs between the conditions when scattered photons are used and when they are not used, whereas the number of incident photons is identical. Therefore, we use the Cramer–Rao lower bound as the accuracy criterion.

The Cramer–Rao lower bound (the variance-covariance matrix) of the k-chained π-junction model is

$$\boldsymbol{V}(k) = \begin{pmatrix} V_{11}(k) & V_{12}(k) \\ V_{21}(k) & V_{22}(k) \end{pmatrix} = \frac{1}{N} \boldsymbol{I}^{-1}(k), \quad (27)$$

where $\boldsymbol{I}(k)$ is the Fisher information matrix.

$$\boldsymbol{I}(k) = \begin{pmatrix} I_{11}(k) & I_{12}(k) \\ I_{21}(k) & I_{22}(k) \end{pmatrix}. \quad (28)$$

Each element of the matrix above is given by

$$\left. \begin{aligned} I_{11}(k) &= -\mathrm{E}\left[\frac{\partial^2}{\partial\mu^2} \log\left(f_k(x, {}^k\boldsymbol{y} \mid \mu, \mu_s)\right)\right], \\ I_{12}(k) &= -\mathrm{E}\left[\frac{\partial^2}{\partial\mu\partial\mu_s} \log\left(f_k(x, {}^k\boldsymbol{y} \mid \mu, \mu_s)\right)\right], \\ I_{21}(k) &= -\mathrm{E}\left[\frac{\partial^2}{\partial\mu_s\partial\mu} \log\left(f_k(x, {}^k\boldsymbol{y} \mid \mu, \mu_s)\right)\right], \\ I_{22}(k) &= -\mathrm{E}\left[\frac{\partial^2}{\partial\mu_s^2} \log\left(f_k(x, {}^k\boldsymbol{y} \mid \mu, \mu_s)\right)\right], \end{aligned} \right\} \quad (29)$$

where N ($N \in \mathbb{N}, 1 \le N$) is the number of independent trials, and $\mathrm{E}[\cdot]$ denotes the expectation operation.

For primary photon-only measurement, as discussed in the previous section, the scattering coefficient μ_s cannot be estimated. Hence, only μ is evaluated independent of k as,

$$V_{prim} = \frac{1}{N \cdot I_{prim}}, \quad (30)$$

$$I_{prim} = -\mathrm{E}\left[\frac{\partial^2}{\partial\mu^2} \log\left(f_{prim}(x \mid \mu)\right)\right]. \quad (31)$$

Thus, we adopted these bounds as the criteria for evaluating accuracy improvement. In particular, because V_{11} corresponds to the variance of the attenuation coefficient μ, it is used as the evaluation index for the estimation accuracy depending on the number k of scatter detectors. By performing differentiation and expectation operations, we obtain the following lemma:

Lemma 1: Let

$$\mathcal{N}_{um}^V(k) = (1 - \exp(-\mu L))\left(1 - \exp\left(-\mu\frac{L}{k}\right)\right)^2 k^2, \quad (32)$$

$$\mathcal{D}_{en}(k) = \left\{ (\mu - \mu_s) \left(1 - \exp\left(-\mu\frac{L}{k}\right)\right)^2 k^2 \exp\left(-\mu L\right) \right.$$
$$\left. + \mu_s \left(1 - \exp\left(-\mu L\right)\right)^2 \exp\left(-\mu\frac{L}{k}\right) \right\} nNL^2. \tag{33}$$

Subsequently, $V_{ij}(k)$, $(i, j \in \{1, 2\})$ is expressed as,

$$V_{11}(k) = \frac{\mu \mathcal{N}^V_{um}(k)}{\mathcal{D}_{en}(k)}, \tag{34}$$

$$V_{12}(k) = V_{21}(k) = \frac{\mu_s \mathcal{N}^V_{um}(k)}{\mathcal{D}_{en}(k)}, \tag{35}$$

$$V_{22}(k) = \frac{\mu_s \mathcal{N}^V_{um}(k)}{\mathcal{D}_{en}(k)} \cdot \left[\frac{L^2 (\mu - \mu_s) \mu_s \exp\left(-\mu\frac{L}{k}\right)}{\left(1 - \exp\left(-\mu\frac{L}{k}\right)\right)^2 k^2} \right.$$
$$\left. + \frac{\mu_s}{\mu} + \frac{L^2 \exp\left(-\mu L\right)}{(1 - \exp\left(-\mu L\right))^2} (\mu - \mu_s)^2 \right], \tag{36}$$

and, V_{prim} is

$$V_{prim} = \frac{1 - \exp(-\mu L)}{nNL^2 \exp(-\mu L)}. \tag{37}$$

The proof of **Lemma 1** is presented in Appendix A.

6. Properties of $V(k)$

6.1 Accuracy Improvement with the Number of Scatter Detector

To present **Theorem 1**, which mentions the properties related to accuracy improvement, we require **Lemma 2**.

Lemma 2: For all t $(t \in \mathbb{R}, 1 \le t)$ and u $(u \in \mathbb{R}, 0 < u)$, the following function is always positive:

$$g(t) = u + u \exp\left(\frac{u}{t}\right) + 2t - 2t \exp\left(\frac{u}{t}\right). \tag{38}$$

This lemma has been proven in [31]. We repeat the proof in Appendix B.

Theorem 1: The following inequality holds for any k, m $(k, m \in \mathbb{N}, 1 \le k < m)$.

$$V_{ij}(k) > V_{ij}(m), \ (i, j \in \{1, 2\}). \tag{39}$$

In particular, for $k = 1$, equation

$$V_{11}(1) = V_{prim} \tag{40}$$

holds.

Proof: (**Theorem 1**) Let $V^{\text{real}}(t)$ be the matrix obtained by replacing the natural number k of $V(k)$ given by **Lemma 1** with real numbers t $(t \in \mathbb{R}, 1 \le t)$. That is,

$$V^{\text{real}}(t) = \begin{pmatrix} V^{\text{real}}_{11}(t) & V^{\text{real}}_{12}(t) \\ V^{\text{real}}_{21}(t) & V^{\text{real}}_{22}(t) \end{pmatrix}. \tag{41}$$

The first derivative of each element of matrix $V^{\text{real}}(t)$ is

$$\frac{d}{dt} V^{\text{real}}_{11}(t) = -\frac{\mu \mu_s \mathcal{N}^d_{um}(t)}{nNL^2 (\mathcal{D}_{en}(t))^2} C(t), \tag{42}$$

$$\frac{d}{dt} V^{\text{real}}_{12}(t) = \frac{d}{dt} V^{\text{real}}_{21}(t) = -\frac{\mu_s^2 \mathcal{N}^d_{um}(t)}{nNL^2 (\mathcal{D}_{en}(t))^2} C(t), \tag{43}$$

$$\frac{d}{dt} V^{\text{real}}_{22}(t) = -\frac{\mu_s^2 \mathcal{N}^d_{um}(t)}{nNL^2 \mu (\mathcal{D}_{en}(t))^2} C(t), \tag{44}$$

where

$$\mathcal{N}^d_{um}(t) = (1 - \exp(-\mu L))^3$$
$$\cdot \left(1 - \exp\left(-\mu\frac{L}{t}\right)\right) \exp\left(-2\mu\frac{L}{t}\right), \tag{45}$$

$$C(t) = \mu L + \mu L \exp\left(\mu\frac{L}{t}\right) + 2t - 2t \exp\left(\mu\frac{L}{t}\right), \tag{46}$$

and $\mathcal{D}_{en}(t)$ is the expression in (33) obtained by substituting k by t. In (42), (43), and (44), $\mathcal{N}^d_{um}(t)$ and $(\mathcal{D}_{en}(t))^2$ are always positive and $C(t)$ is also positive as it is obtained by substituting u by μL in **Lemma 2**. Therefore, we have

$$\frac{d}{dt} V^{\text{real}}_{ij}(t) < 0, \ (i, j \in \{1, 2\}). \tag{47}$$

Thus, each element of the matrix $V^{\text{real}}(t)$ is a strictly monotonically decreasing function. Because k, m is an element of the set $\{t \in \mathbb{R} \mid 1 \le t\}$, when $k < m$, we conclude that

$$V_{ij}(k) > V_{ij}(m), \ (i, j \in \{1, 2\}). \tag{48}$$

Furthermore, substituting k by 1 in (34) yields

$$V_{11}(1) = \frac{1 - \exp(-\mu L)}{nNL^2 \exp(-\mu L)}. \tag{49}$$

The right-hand sides of (49) and (37) are equal, implying that (40) holds. □

This theorem implies the following.

- If the number of scatter detectors is two or more, the estimation accuracy of only primary photons is exceeded, where the accuracy can be further improved as the number of detectors is increased.
- However, if only one scatter detector ($k = 1$) is available, no improvement in accuracy is observed even if scattered photons are detected.

6.2 Effects of Photoelectric Absorption

The coefficient μ_s represents the scattering ratio in the interaction, where a small value indicates large photoelectric absorption. Here, we show that the accuracy of the attenuation coefficient estimation is high when the photoelectric absorption is low. Consequently, the following theorem holds.

Theorem 2: For all k $(k \in \mathbb{N}, 1 \le k)$, $V_{11}(k)$ decreases monotonically with respect to μ_s, $(0 \le \mu_s \le \mu)$.

Proof: (**Theorem 2**) The theorem holds when the following inequality holds:

TODA and NAKAGAMI: PRINCIPLE ANALYSIS FOR THE POSSIBILITY OF SCATTERED X-RAY TO IMPROVE COMPUTED TOMOGRAPHY RECONSTRUCTION

7

$$\frac{dV_{11}(k)}{d\mu_s} \le 0, \ (0 \le \mu_s \le \mu). \tag{50}$$

The equality holds when $k = 1$. $V_{11}(k)$ can be rewritten as

$$
\begin{aligned}
V_{11}(k) &= \frac{\mu \mathcal{N}_{\text{um}}^V(k)}{\mathcal{D}\text{en}(k)} \\
&= \frac{\mu(1 - P_{prim})}{nNL^2} \frac{(1 - p_k)^2 k^2}{\mu(1 - p_k)^2 k^2 P_{prim} + \mu_s \mathcal{J}},
\end{aligned} \tag{51}
$$

where

$$\mathcal{J} = (1 - P_{prim})^2 p_k - (1 - p_k)^2 k^2 P_{prim}. \tag{52}$$

As $P_{prim}, n, N, L, k, p_k$ and μ are positive constants, we need only that $\mathcal{J} \ge 0$ for (50) to hold. Using the relationship between the arithmetic and geometric means [34], we have the following inequality:

$$\frac{1 + p_k + p_k^2 + \cdots + (p_k)^{k-1}}{k} \ge \left(\prod_{\ell=1}^{k} (p_k)^{\ell-1}\right)^{\frac{1}{k}}. \tag{53}$$

The equality holds when $k = 1$ or $p_k = 1$; however, the latter is excluded because $0 < p_k < 1$. Since the right-hand side of the inequality (53) can be expressed as

$$\left(\prod_{\ell=1}^{k} (p_k)^{\ell-1}\right)^{\frac{1}{k}} = \left(p_k^{\frac{k(k-1)}{2}}\right)^{\frac{1}{k}} = p_k^{\frac{k-1}{2}}, \tag{54}$$

we have

$$\frac{1 + p_k + p_k^2 + \cdots + (p_k)^{k-1}}{k} \ge p_k^{\frac{k-1}{2}}. \tag{55}$$

Multiplying both sides of the inequality by $(1 - p_k)$ and then squaring and using $(p_k)^k = P_{prim}$ yields

$$
\begin{aligned}
(1 - p_k)^2 &\left(1 + p_k + p_k^2 + \cdots + (p_k)^{k-1}\right)^2 \\
&\ge (1 - p_k)^2 k^2 (p_k)^{k-1} \\
(1 - P_{prim})^2 &\ge (1 - p_k)^2 k^2 (p_k)^{k-1}.
\end{aligned} \tag{56}
$$

Finally, by multiplying both sides by p_k, we obtain

$$(1 - P_{prim})^2 p_k \ge (1 - p_k)^2 k^2 P_{prim}. \tag{57}$$

Thus,

$$\mathcal{J} = (1 - P_{prim})^2 p_k - (1 - p_k)^2 k^2 P_{prim} \ge 0. \tag{58}$$

$\square$

When $\mu_s = 0$, that is, when all interacting photons are photoelectrically absorbed, by substituting μ_s by 0 in (51), $V_{11}(k)$ becomes a constant for k given by,

$$V_{11}(k)|_{\mu_s=0} = \frac{1 - \exp(-\mu L)}{nNL^2 \exp(-\mu L)}. \tag{59}$$

$V_{11}(k)|_{\mu_s=0}$ is equal to V_{prim} given by (37), that is, the estimated variance from the primary photon-only measurements.

However, when $\mu_s = \mu$, that is, in a situation where all interacting photons are scattered, $V_{11}(k)$ achieves the minimum given by,

$$V_{11}(k)|_{\mu_s=\mu} = \frac{\left(1 - \exp\left(-\mu \frac{L}{k}\right)\right)^2 k^2}{nNL^2(1 - \exp(-\mu L)) \exp\left(-\mu \frac{L}{k}\right)}. \tag{60}$$

This case is consistent with that in the literature [31] for situations without photoelectric absorption.

Thus, studies have shown that even if photons are annihilated during photoelectric absorption, the accuracy of estimating the attenuation coefficient can be improved by measuring the scattered photons.

6.3 Limit to accuracy improvement

As $V_{ij}(k)$ decreases monotonically with respect to k and is positive, it converges to its limit. This limit corresponds to the extent to which accuracy can be improved by increasing the number of scatter detectors. The limit of each $V_{ij}(k)$ as k approaches infinity is expressed as,

Let

$$\mathcal{F} = \mu^2 \left(1 - \exp(-\mu L)\right), \tag{61}$$

$$
\begin{aligned}
\mathcal{G} = nN \big[&(\mu - \mu_s) \mu^2 L^2 + \mu_s \left(\exp(-\mu L)\right. \\
&\left. + \exp(\mu L) - 2\right) \big] \exp(-\mu L),
\end{aligned} \tag{62}
$$

$$
\begin{aligned}
\mathcal{H} = nN \big[&(\mu - \mu_s) \mu^2 L^2 \exp(-\mu L) \\
&+ \mu_s \left(1 - \exp(-\mu L)\right)^2 \big],
\end{aligned} \tag{63}
$$

then the limits can be expressed as,

$$\lim_{k \to \infty} V_{11}(k) = \frac{\mu \mathcal{F}}{\mathcal{G}}, \tag{64}$$

$$\lim_{k \to \infty} V_{21}(k) = \lim_{k \to \infty} V_{12}(k) = \frac{\mu_s \mathcal{F}}{\mathcal{G}}, \tag{65}$$

$$
\begin{aligned}
\lim_{k \to \infty} V_{22}(k) &= \frac{\mu_s \mathcal{F}}{\mathcal{H}} \\
&\cdot \left[\frac{(2\mu - \mu_s) \mu_s}{\mu^2} + \frac{L^2 \exp(-\mu L)}{(1 - \exp(-\mu L))^2} (\mu - \mu_s)^2\right].
\end{aligned} \tag{66}
$$

where we use the following well-known formula for the limit:

$$\lim_{\eta \to 0} \frac{\exp(\eta) - 1}{\eta} = 1, \ \ (\eta \in \mathbb{R}). \tag{67}$$

Using this formula, the limits (64), (65), and (66) are derived by substituting η for $\frac{\mu L}{k}$ in (34), (35), and (36) respectively.

7. Numerical experiment

In this section, we performed a numerical experiment to verify the effect of using scattered photons on the geometry of

the homogeneous thin cylinder shown in Fig. 3. To obtain the projection data, we employed a Monte Carlo method provided in EGS5 [35]. Using these measured data, the attenuation coefficient was estimated with a maximum likelihood method [33].

7.1 Maximum likelihood estimator for homogeneous thin cylinder

We constructed the k-chained π-junction model as a model of homogenous thin cylinder, and derived its probability function (24). Therefore, a maximum likelihood method for estimating the attenuation coefficient of a thin cylinder using this model can be developed.

Let the number of photons measured by each sensor in the j-th $(1 \le j \le N)$ trial be $\left(x^{(j)}, {}^k\boldsymbol{y}^{(j)}\right)$, where ${}^k\boldsymbol{y}^{(j)} = \left(y_1^{(j)}, y_2^{(j)}, \cdots, y_k^{(j)}\right)$. The likelihood function is given by,

$$
\begin{aligned}
&\mathcal{L}_k\left(\mu, \mu_s \mid x^{(j)}, {}^k\boldsymbol{y}^{(j)}\right) \\
&\quad = f_k(x, {}^k\boldsymbol{y} \mid \mu, \mu_s)\big|_{(x, {}^k\boldsymbol{y}) = (x^{(j)}, {}^k\boldsymbol{y}^{(j)})}.
\end{aligned}
\tag{68}
$$

Log likelihood with N times independent trails becomes

$$
J(\mu, \mu_s) = \log\left[\prod_{j=1}^{N} \mathcal{L}_k\left(\mu, \mu_s \mid x^{(j)}, {}^k\boldsymbol{y}^{(j)}\right)\right],
\tag{69}
$$

where, $\log \mathcal{L}_k\left(\mu, \mu_s \mid x^{(j)}, {}^k\boldsymbol{y}^{(j)}\right)$ is identical to (A· 2).

Maximization of $J(\mu, \mu_s)$ is achieved by (μ, μ_s) that satisfies

$$
\begin{cases}
\dfrac{\partial}{\partial \mu} J(\mu, \mu_s) & = 0, \\[2mm]
\dfrac{\partial}{\partial \mu_s} J(\mu, \mu_s) & = 0.
\end{cases}
\tag{70}
$$

Equation (70) is rewritten as,

$$
\begin{cases}
-L\mathcal{X} - \dfrac{L}{k}\displaystyle\sum_{i=1}^{k}(i-1)\mathcal{Y}_i + \dfrac{L\exp\left(-\mu\frac{L}{k}\right)}{k\left[1-\exp\left(-\mu\frac{L}{k}\right)\right]}\displaystyle\sum_{i=1}^{k}\mathcal{Y}_i \\[3mm]
\quad -\dfrac{1}{\mu}\displaystyle\sum_{i=1}^{k}\mathcal{Y}_i + \left(\dfrac{L\exp\left(-\mu L\right)}{1-\exp(-\mu L)} + \dfrac{\mu_s}{(\mu-\mu_s)\mu}\right)\mathcal{Z} = 0, \\[3mm]
\dfrac{1}{\mu_s}\displaystyle\sum_{i=1}^{k}\mathcal{Y}_i - \dfrac{1}{\mu-\mu_s}\mathcal{Z} \qquad\qquad = 0,
\end{cases}
\tag{71}
$$

where,

$$
\mathcal{X} = \sum_{j=1}^{N} x^{(j)}, \quad \mathcal{Y}_i = \sum_{j=1}^{N} y_i^{(j)}, \quad \mathcal{Z} = nN - \mathcal{X} - \sum_{i=1}^{k} \mathcal{Y}_i.
\tag{72}
$$

Eliminating μ_s in (71), we obtain

$$
\begin{aligned}
h(\mu) = &-L\mathcal{X} - \frac{L}{k}\sum_{i=1}^{k}(i-1)\mathcal{Y}_i + \frac{L\exp\left(-\mu\frac{L}{k}\right)}{k\left[1-\exp\left(-\mu\frac{L}{k}\right)\right]}\sum_{i=1}^{k}\mathcal{Y}_i \\
&+ \frac{L\exp\left(-\mu L\right)}{1-\exp(-\mu L)}\mathcal{Z} = 0.
\end{aligned}
\tag{73}
$$

To solve equation $h(\mu) = 0$, we employ the Newton-Raphson method. The derivative of $h(\mu)$ is given as,

$$
\begin{aligned}
\frac{d}{d\mu}h(\mu) = &\frac{L^2 \exp\left(-\mu\frac{L}{k}\right)}{k^2\left[1-\exp\left(-\mu\frac{L}{k}\right)\right]^2}\sum_{i=1}^{k}\mathcal{Y}_i \\
&+ \frac{L^2\exp(-\mu L)}{[1-\exp(-\mu L)]^2}\mathcal{Z}.
\end{aligned}
\tag{74}
$$

By denoting attenuation coefficients before and after renewal as μ^{old} and μ^{new}, respectively, the renewal equation for the Newton-Raphson method is given by,

$$
\mu^{new} = \mu^{old} - \frac{h\left(\mu^{old}\right)}{\frac{d}{d\mu}h(\mu)\big|_{\mu=\mu^{old}}}.
\tag{75}
$$

After sufficient number of renewal iterations, the converged value will be adopted as the estimated attenuation coefficient $\widehat{\mu}$. Estimation value of scattering coefficient $\widehat{\mu_s}$ is given as,

$$
\widehat{\mu_s} = \frac{\displaystyle\sum_{i=1}^{k}\mathcal{Y}_i}{nN - \mathcal{X}}\widehat{\mu}.
\tag{76}
$$

In carrying out M_{mc} times Monte Carlo simulations, let the m-th $(1 \le m \le M_{mc})$ estimated attenuation coefficient be denoted as $\widehat{\mu}^{(m)}$. Then its estimated variance $\widehat{V_\mu}$ is given by,

$$
\widehat{V_\mu} = \frac{1}{M_{mc}}\sum_{m=1}^{M_{mc}}\left(\widehat{\mu}^{(m)} - \overline{\widehat{\mu}}\right)^2,
\tag{77}
$$

where,

$$
\overline{\widehat{\mu}} = \frac{1}{M_{mc}}\sum_{m=1}^{M_{mc}}\widehat{\mu}^{(m)}.
\tag{78}
$$

7.2 Monte Carlo simulation

In this section, we estimate $\widehat{V_\mu}$ using the maximum likelihood method introduced in the previous section for the measured number of photons obtained from Monte Carlo simulation implemented in EGS5, and compare the variance of these estimated values with theoretical values given in **Lemma 1**.

The material of homogeneous thin cylinder was water. The diameter and the length of the cylinder was 5.0×10^{-5}, and 5.0 cm, respectively. The maximum number of NaI toroidal scatter detectors $\ell_{\max}$ was set to 10. The inside and outside diameters of the toroidal scatter detectors were 5.125×10^{-5} and 5.0×10^{-4} cm, respectively. Primary photons were measured with an ordinary cylindrical NaI detector of diameter and length 5.0×10^{-4}, 5.0×10^{-4} cm, respectively. The X-ray source, the thin cylinder, and the primary detector were placed collinearly. The distance from the origin of the X-ray source to the center of the thin cylinder was 11.0cm, and the distance from the center of the thin cylinder to the primary detecter was 11.05cm. The number of photons n used to collect the projection data at a single energy of 20 keV was set to 10^5, and the independent trial number N

TODA and NAKAGAMI: PRINCIPLE ANALYSIS FOR THE POSSIBILITY OF SCATTERED X-RAY TO IMPROVE COMPUTED TOMOGRAPHY RECONSTRUCTION

9

Table 1 Estimated $\widehat{\mu}$ and $\widehat{V_\mu}$

k	$\widehat{\mu}$	$\widehat{V_\mu}$
1	8.35798×10^{-1}	2.44832×10^{-6}
2	8.35843×10^{-1}	1.62018×10^{-6}
3	8.35881×10^{-1}	1.52615×10^{-6}
4	8.35813×10^{-1}	1.34417×10^{-6}
5	8.35820×10^{-1}	1.38168×10^{-6}
6	8.35829×10^{-1}	1.39326×10^{-6}
7	8.35757×10^{-1}	1.35447×10^{-6}
8	8.35791×10^{-1}	1.30286×10^{-6}
9	8.35749×10^{-1}	1.34248×10^{-6}
10	8.35812×10^{-1}	1.27347×10^{-6}

$$\mu^* = 8.35817 \times 10^{-1}$$

Fig. 6 Numerical example of $V_{11}(k)$ versus k

was set to 10. The number of Monte Carlo simulation M_{mc} was set to 1024.

As the desired value of attenuation coefficient, we adopted $\mu^* = 8.35817 \times 10^{-1}$ which was calculated from Monte Carlo simulation using the primary detector of homogenious thin cylinder geometry of $k = 1$ with a sufficiently large number $(n \cdot N = 10^{10})$ of photons. According to V_{prim}, the standard deviation in this case is approximately 1.60×10^{-5}, the desired value is accurate to about five decimal places. Similarly, the desired value of scatter coefficient is given as $\mu_s^* = 2.94452 \times 10^{-1}$ using the measured numbers of photons both primary and scatter detector of the same geometry and number of incident photons.

Table 1 lists estimated $\widehat{\mu}$ and $\widehat{V_\mu}$ for each k. The estimated $\widehat{\mu}$ s are very close to the desired value μ^*. In Fig. 6, the horizontal axis represents the number k of scatter detector, the vertical axis represents the variance, and the thick line with a center symbol represents the estimated variance $\widehat{V_\mu}$ of the attenuation coefficient. The thin line overlapping the estimated value is the theoretical value obtained by substituting the above geometrical constants and desired values into the corresponding variables of $V_{11}(k)$ in (34), and the thin line parallel to the horizontal axis close to this is the limiting value of (64). When the number of scatter detectors is $k = 1$, even when scattered photons are measured, $V_{11}(k)$ is equal to V_{prim}. As the number of scatter detectors increased, the variance monotonically decreased and approached $\lim_{k \to \infty} V_{11}(k)$. The theoretical values explain well the results of numerical experiments using Monte Carlo simulations.

The thin curved line labeled $V_{11}(k)|_{\mu_s = \mu}$ is the theoretical value when all photons except the primary photon are assumed to be scattered, i.e., when there is no photoelectric absorption, and the straight line indicates $\lim_{k \to \infty} V_{11}(k)|_{\mu_s = \mu}$. This value is considered to be a lower limit of the variance. As shown in Theorem 2, the results under the conditions of the numerical experiment lie between this lower bound and the estimated variance using only primary photons. In this case, substituting μ^* and μ_s^* into (3), the corresponding coefficient of photoelectric absorption μ_a is determined as 5.41364×10^{-1}. Approximately 64.8% of interacting photons are absorbed. Although a considerable number of photons are lost, the accuracy is greatly improved compared
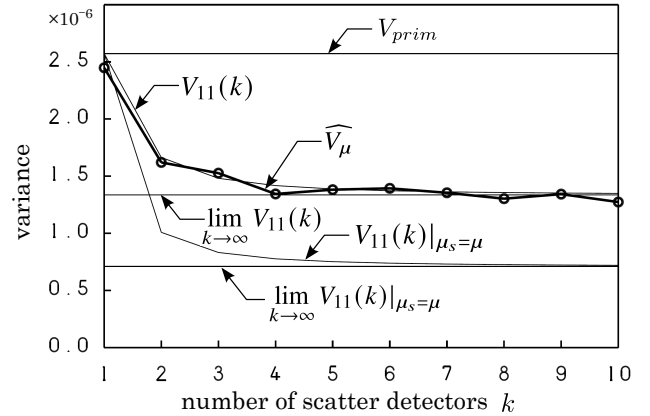
to measurements of primary photon only.

Thus, using two or more scatter detectors, the accuracy of estimating the attenuation coefficient can be improved despite existence of photoelectric absorption.

8. Conclusions and discussion

Scattered X-rays have been eliminated as an unnecessary entity that causes harm to CT reconstruction. However, we investigated the question related to the necessity of scattered X-rays from a statistical perspective. In this study, we introduced the effect of photoelectric absorption into a simplified model termed the k-chained π-junction model for a homogeneous thin cylinder. As a criterion for evaluating the accuracy, the variance of the estimated values was analyzed using the Cramer–Rao lower bound. The estimated variance of the attenuation coefficient decreased with an increase in the number of scatter detectors. However, as the amount of photoelectric absorption increased, the degree of accuracy improvement decreased, but the accuracy was higher than when no scattered X-rays were measured. Therefore, even if photoelectric absorption occurs, the accuracy of estimating the attenuation coefficient can be improved by measuring the scattered and primary X-rays. The presented results of the numerical experiments support this finding.

Future studies will include the introduction of X-ray energy into the model, thus enabling building a foundation for using scattered X-rays in spectral CT. In addition, some efficient methods that use scattered X-rays should be developed by leveraging recent computer capabilities.

Appendix A: Proof of **Lemma 1**

In the support set $\mathbb{S}_{f_k}$, the expected value of $\phi(x, {}^k\boldsymbol{y})$ is given by

$$E\left[\phi(x, {}^{k}\boldsymbol{y})\right] = \sum_{(x,{}^{k}\boldsymbol{y})\in\mathbb{S}_{f_{k}}} \phi(x, {}^{k}\boldsymbol{y}) f_{k}(x, {}^{k}\boldsymbol{y} \mid \mu, \mu_{s}). \tag{A·1}$$

Taking logarithms of both sides of (24), we have

$$\log\left\{f_{k}(x, {}^{k}\boldsymbol{y} \mid \mu, \mu_{s})\right\}$$

$$= \log\left\{\frac{n!}{x!\left(n-x-\sum\limits_{i=1}^{k}y_{i}\right)!\prod\limits_{i=1}^{k}y_{i}!}\right\} - \mu Lx$$

$$-\frac{\mu L}{k}\sum_{i=1}^{k}(i-1)y_{i} + \left(\sum_{i=1}^{k}y_{i}\right)\log\left\{1-\exp\left(-\mu\frac{L}{k}\right)\right\}$$

$$+\left(\sum_{i=1}^{k}y_{i}\right)\log\left\{\frac{\mu_{s}}{\mu}\right\}$$

$$+\left(n-x-\sum_{i=1}^{k}y_{i}\right)\log\left\{1-\exp\left(-\mu L\right)\right\}$$

$$+\left(n-x-\sum_{i=1}^{k}y_{i}\right)\log\left\{1-\frac{\mu_{s}}{\mu}\right\}. \tag{A·2}$$

Consequently, each element of the Fisher information matrix (29) becomes

$$I_{11}(k) = -E\left[\frac{\partial^{2}}{\partial\mu^{2}}\log\left\{f_{k}(x, {}^{k}\boldsymbol{y} \mid \mu, \mu_{s})\right\}\right]$$

$$= \frac{L^{2}\exp\left(-\mu\frac{L}{k}\right)}{k^{2}\left(1-\exp\left(-\mu\frac{L}{k}\right)\right)^{2}}\sum_{i=1}^{k}E\left[y_{i}\right] - \frac{1}{\mu^{2}}\sum_{i=1}^{k}E\left[y_{i}\right]$$

$$+ \frac{L^{2}\exp\left(-\mu L\right)}{(1-\exp\left(-\mu L\right))^{2}}\left(n-E\left[x\right]-\sum_{i=1}^{k}E\left[y_{i}\right]\right)$$

$$+ \frac{(2\mu-\mu_{s})\mu_{s}}{(\mu_{s}-\mu)^{2}\mu^{2}}\left(n-E\left[x\right]-\sum_{i=1}^{k}E\left[y_{i}\right]\right), \tag{A·3}$$

$$I_{12}(k) = -E\left[\frac{\partial^{2}}{\partial\mu\mu_{s}}\log\left\{f_{k}(x, {}^{k}\boldsymbol{y} \mid \mu, \mu_{s})\right\}\right]$$

$$= \frac{1}{(\mu_{s}-\mu)^{2}}\left(n-E\left[x\right]-\sum_{i=1}^{k}E\left[y_{i}\right]\right), \tag{A·4}$$

$$I_{21}(k) = -E\left[\frac{\partial^{2}}{\partial\mu_{s}\mu}\log\left\{f_{k}(x, {}^{k}\boldsymbol{y} \mid \mu, \mu_{s})\right\}\right]$$

$$= \frac{1}{(\mu_{s}-\mu)^{2}}\left(n-E\left[x\right]-\sum_{i=1}^{k}E\left[y_{i}\right]\right), \tag{A·5}$$

$$I_{22}(k) = -E\left[\frac{\partial^{2}}{\partial\mu_{s}^{2}}\log\left\{f_{k}(x, {}^{k}\boldsymbol{y} \mid \mu, \mu_{s})\right\}\right]$$

$$= \frac{1}{\mu_{s}^{2}}\sum_{i=1}^{k}E\left[y_{i}\right] + \frac{1}{(\mu_{s}-\mu)^{2}}\left(n-E\left[x\right]-\sum_{i=1}^{k}E\left[y_{i}\right]\right). \tag{A·6}$$

Because $E[x]$ and $\sum\limits_{i=1}^{k}E[y_{i}]$ in the above equations are given by

$$E[x] = n\exp(-\mu L), \tag{A·7}$$

$$\sum_{i=1}^{k}E\left[y_{i}\right] = \sum_{i=1}^{k}n\exp\left(-\mu(i-1)\frac{L}{k}\right)$$

$$\cdot\left(1-\exp\left(-\mu\frac{L}{k}\right)\right)\frac{\mu_{s}}{\mu}$$

$$= \frac{n\mu_{s}}{\mu}\left(1-\exp\left(-\mu L\right)\right), \tag{A·8}$$

Substituting these expressions into (A·3)−(A·6), we obtain

$$I_{11}(k) = \frac{nL^{2}\mu_{s}\left(1-\exp\left(-\mu L\right)\right)}{k^{2}\mu\left(1-\exp\left(-\mu\frac{L}{k}\right)\right)^{2}}\exp\left(-\mu\frac{L}{k}\right)$$

$$-\frac{n\mu_{s}}{\mu^{3}}\left(1-\exp\left(-\mu L\right)\right)$$

$$+\frac{nL^{2}\exp\left(-\mu L\right)}{1-\exp\left(-\mu L\right)}\left(1-\frac{\mu_{s}}{\mu}\right)$$

$$+\frac{n\left(2\mu-\mu_{s}\right)\mu_{s}}{\left(\mu-\mu_{s}\right)\mu^{3}}\left(1-\exp\left(-\mu L\right)\right), \tag{A·9}$$

$$I_{12}(k) = -\frac{n\left(1-\exp\left(-\mu L\right)\right)}{\left(\mu-\mu_{s}\right)\mu}, \tag{A·10}$$

$$I_{21}(k) = -\frac{n\left(1-\exp\left(-\mu L\right)\right)}{\left(\mu-\mu_{s}\right)\mu}, \tag{A·11}$$

$$I_{22}(k) = \frac{n\left(1-\exp\left(-\mu L\right)\right)}{\left(\mu-\mu_{s}\right)\mu_{s}}. \tag{A·12}$$

Using these elements, the determinant of Fisher information matrix $|\boldsymbol{I}(k)|$ is shown to be positive (not zero) as follows:

$$|\boldsymbol{I}(k)| = I_{11}(k)I_{22}(k) - I_{12}(k)I_{21}(k)$$

$$= \frac{n^{2}L^{2}}{\mu_{s}\mu\left(\mu-\mu_{s}\right)\left(1-\exp\left(-\mu\frac{L}{k}\right)\right)^{2}k^{2}}$$

$$\cdot\left[\left(\mu-\mu_{s}\right)\left(1-\exp\left(-\mu\frac{L}{k}\right)\right)^{2}k^{2}\exp\left(-\mu L\right)\right.$$

$$\left.+ \mu_{s}\left(1-\exp\left(-\mu L\right)\right)^{2}\exp\left(-\mu\frac{L}{k}\right)\right] > 0. \tag{A·13}$$

Thus, $\boldsymbol{I}(k)$ is an inverse matrix. Based on these results, we obtain (34)−(36).

V_{prim} in (30) is expressed as follows:

$$V_{prim} = -\frac{1}{N\cdot E\left[\frac{\partial^{2}}{\partial\mu^{2}}\log\left(f_{prim}(x|\mu)\right)\right]}. \tag{A·14}$$

Substituting (26) into the above equation, the expression

$$V_{prim} = \frac{1}{\frac{NL^{2}\exp(-\mu L)}{(1-\exp(-\mu L))^{2}}\left(n-E[x]\right)}$$

$$= \frac{1-\exp(-\mu L)}{nNL^{2}\exp(-\mu L)} \tag{A·15}$$

TODA and NAKAGAMI: PRINCIPLE ANALYSIS FOR THE POSSIBILITY OF SCATTERED X-RAY TO IMPROVE COMPUTED TOMOGRAPHY RECONSTRUCTION

11

is obtained.   □

Appendix B: Proof of **Lemma 2**

The first derivative of the function $g(t)$ $(1 \leq t)$ strictly increases.

$$\frac{d}{dt}g(t) = 2 - \frac{2t^2 - 2ut + u^2}{t^2} \exp\left(\frac{u}{t}\right). \qquad (A \cdot 16)$$

This is because, for all $t \geq 1$ and $u > 0$,

$$\frac{d^2}{dt^2}g(t) = \frac{u^3}{t^4} \exp\left(\frac{u}{t}\right) > 0. \qquad (A \cdot 17)$$

Moreover, the limits of (38) and (A·16) as t approaches infinity are as given by
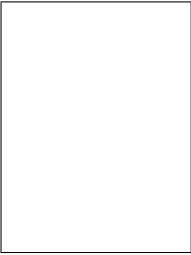
$$\lim_{t \to \infty} g(t) = 0, \qquad (A \cdot 18)$$

$$\lim_{t \to \infty} \frac{d}{dt}g(t) = 0. \qquad (A \cdot 19)$$

Therefore, (A·16) is always negative; that is, $\frac{d}{dt}g(t) < 0$. Consequently, because $g(t)$ is a strictly decreasing function, the function $g(t)$ in (A·18) is always positive; that is, $g(t) > 0$.

□

References
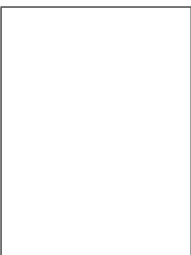
[1] J. Hsieh, Computed Tomography: Principles, Design, Artifacts and Recent Developements, 4th ed. Bellingham, Washington, USA). SPIE Press, 2022.

[2] J. Potočnik, S. Foley and E. Thomas, "Current and potential applications of artificial intelligence in medical imaging practice: A narrative review," Journal of Medical Imaging and Radiation Sciences, vol.54, pp.376–385, Apr. 14, 2023. DOI:10.1016/j.jmir.2023.03.033

[3] R. Booij, R. P. J. Budde, M. L. Dijkshoorn and M. van Straten, "Technological developments of X-ray computed tomography over half a century: User's influence on protocol optimization, European Journal of Radiology, vol.131, 109261, Aug. 2020. DOI:10.1016/j.ejrad.2020.109261

[4] H. Kanamori, N. Nakamori, K. Inoue and E. Takenaka, "Effects of scattered x-rays on CT images," Physics in Medicine and Biology, vol.30, no.3, pp.239–249, Mar. 1985. DOI:10.1088/0031-9155/30/3/004

[5] K. Tokumoto, Y. Yamazaki, N. Toda and S. Koyama, "Evaluation of scattered radiation in cone-beam dual-energy X-ray CT with Monte Carlo simulation," The Radiological Society of North America (RSNA) 98th Scientific Assembly and Annual Meeting, SSG16-02, Nov. 2013.

[6] K. Yiannis and K. Willi, "Efficiency of antiscatter grids for flat-detector CT," Physics in Medicine and Biology, vol. 52, no. 20, pp.6275–6293, Oct. 2007. DOI:10.1088/0031-9155/52/20/013

[7] Lei Zhu, Yaogin Xie, Jiang Wang and Lei Xing, "Scatter correction for cone-beam CT in radiation therapy," Medical Physics, vol. 36, no. 6, pp.2258–2268, May 2009. DOI:10.1118/1.3130047

[8] A. Akbarzadeh, M.R. Ay, H. Sarkar and H. Zaidi, "Measurement of scattered radiation in a volumetric 64-slice CT scanner using three experimental techniques," Physics in Medicine and Biology, vol. 55, No. 8, pp.2269–2280, Mar. 2010. DOI:10.1088/0031-9155/55/8/010

[9] H. Yan, X. Mou, S. Tang, Q. Xu and M. Zankl, "Projection correlation based view interpolation for cone beam CT: primary fluence restoration in scatter measurement with a moving beam stop array," Physics in Medicine and Biology, vol. 55, no. 21,pp.6353–6375, Oct.

2010. DOI:10.1088/0031-9155/55/21/002

[10] W. Zhao, S. Brunner, K. Niu, S. Schafer, K. Royalty and G.H. Chen, "Patient-specific scatter correction for flat-panel detector-based cone-beam CT imaging," Physics in Medicine and Biology, vol. 60, no. 3, pp.1339–1365, Jan. 2015. DOI:10.1088/0031-9155/60/3/1339

[11] M. Baer and M. Kachelrieß, "Hybrid scatter correction for CT imaging," Physics in Medicine and Biology, vol. 57, no. 21, pp.6849–6867, Oct. 2012. DOI:10.1088/0031-9155/57/21/6849

[12] G. Jarry, S.A. Graham, D.J. Moseley, D.J. Jaffray, J.H. Siewerdsen and F. Verhaegen, "Characterization of scattered radiation in kV CBCT images using Monte Carlo simulations," Medical Physics, vol. 33, no. 11, pp.4320–4329, Oct. 2006. DOI:10.1118/1.2358324

[13] Y. Xu, T. Bai, H. Yan, L. Ouyang, A. Pompos, J. Wang, L. Zhou, S.B. Jiang and X. Jia, "A practical cone-beam CT scatter correction method with optimized Monte Carlo simulations for image-guided radiation therapy," Physics in Medicine and Biology, vol. 60, no. 9, pp.3567–3587, Apr. 2015. DOI:10.1088/0031-9155/60/9/3567

[14] G.J. Bootsma, F. Verhaegen and D.A. Jaffray, "Efficient scatter distribution estimation and correction in CBCT using concurrent Monte Carlo fitting," Medical Physics, vol. 42, No. 1, pp.54–68, Jan. 2015. DOI:10.1118/1.4903260

[15] T.T. Truong and M.K. Nguyen,"Recent developments in compton scatter tomography: Theory and numerical simulations." Numerical Simulation - From Theory to Industry, INTECH Open Access Publisher, ch. 6, pp.101–128, Sep. 2012. DOI:10.5772/50012

[16] P.G. Lale, "The examination of internal tissues, using gamma-ray scatter with a possible extension to megavoltage radiography," Physics in Medicine and Biology, vol. 4, no. 2, pp.159–167, 1959. DOI: 10.1088/0031-9155/4/2/305

[17] J.J. Battista, and M.J. Bronskill, "Compton scatter imaging of transverse sections: an overall appraisal and evaluation for radiotherapy planning," Physics in Medicine and Biology, vol. 26, no. 1, pp.81–99, Jan. 1981. DOI:10.1088/0031-9155/26/1/009

[18] S.J. Norton, "Compton scattering tomography." Journal of Applied Physics, vol. 76, no. 4, pp.2007–2015, Aug. 1994. DOI:10.1063/1.357668

[19] M.K. Nguyen, T.T. Truong, M. Morvidone and H. Zaidi, "Scattered radiation emission imaging: Principles and applications," Journal of Biomedical Imaging, vol. 2011, pp.13–28, Jun. 2011. DOI:10.1155/2011/913893

[20] F. Zhao, J.C. Schotland and V.A. Markel, "Inversion of the star transform," Inverse Problems, vol. 30, no. 10, pp.105001–105032, Oct. 2014. DOI:10.1088/0266-5611/30/10/105001

[21] R. Krylov and A. Katsevich, "Inversion of the broken ray transform in the case of energy-dependent attenuation," Physics in Medicine and Biology, vol. 60, no. 11, pp.4313–4334, May 2015. DOI:10.1088/0031-9155/60/11/4313

[22] T.T. Truong and M.K. Nguyen, "New properties of the V-line Radon transform and their imaging applications," Journal of Physics A: Mathematical and Theoretical, vol. 48, no. 40, pp.405204–405232, Sep. 2015. DOI:10.1088/1751-8113/48/40/405204

[23] J.B. Thaibault, K.D. Sauer, C.A. Bouman and J. Hsieh, "A three-dimensional statistical approach to improved image quality for multislice helical CT," Medical Physics, vol. 34, No. 11, pp.4526–4544, Oct. 2007. DOI:10.1118/1.2789499

[24] Z. Yu, J.B. Thaibault, C.A. Bouman, K.D. Sauer and J. Hsieh, "Fast model-based X-ray CT reconstruction using spatially nonhomogeneous ICD Optimization," IEEE Transaction on Image Processing, vol. 20, no. 1, pp.161–175, Jan. 2011. DOI:10.1109/TIP.2010.2058811

[25] K. Yasaka, M. Katsura, M. Akahane, J. Sato, I. Matsuda and K. Ohtomo, "Model-based iterative reconstruction for reduction of radiation dose in abdominopelvic CT: comparison to adaptive statistical iterative reconstruction," SpringerPlus, vol. 2, no. 209, May 2013. DOI:10.1186/2193-1801-2-209

[26] D. Nagae and N. Toda, "Reconstruction accuracy of X-ray computed tomography introduced scattered X-rays measurement," IEICE

Trans. Information & Systems (Japanese Edition), Vol. J101-D, No. 8, pp.1200–1208, Aug. 2018. Online ISSN:1881-0225

[27] M.Z. Alom , T. M. Taha, C. Yakopcic, S. Westberg, P. Sidike, M. S. Nasrin, M. Hasan, B.C. Van Essen, A.A.S. Awwal and V.K. Asari,"A State-of-the-Art Survey on Deep Learning Theory and Architectures," Electronics, vol. 8, no. 292, Mar. 2019. DOI:10.3390/electronics8030292

[28] G. Wang, J. C. Ye and B. D. Man, "Deep learning for tomographic image reconstruction," Nature Machine Intelligence, vol. 2, pp.737–748, Dec. 2020. DOI:10.1038/s42256-020-00273-z

[29] H. Shan, A. Padole, F. Homayounieh, U. Kruger, R. D. Khera, C. Nitiwarangkul, M. K. Kalra and G. Wang,"Competitive performance of a modularized deep neural network compared to commercial algorithms for low-dose CT image reconstruction," Nature Machine Intelligence, vol. 1, pp.269–276, Jun. 2019. DOI:10.1038/s42256-019-0057-9

[30] S. Ito and N. Toda,"Improvement of CT reconstruction using scattered X-rays," IEICE Trans. inf. & syst., vol. E104–D, no. 8, pp.1378–1385, Aug. 2021. DOI:10.1587/transinf.2020EDP7241

[31] N. Toda, T. Nakagami, Y. Yamazaki, H. Yoshioka and S. Koyama, "Using scattered X-rays to improve the estimation accuracy of attenuation coefficients: a fundamental analysis," IEICE Trans. Fundamentals, vol. E101-A, no. 7, pp.1101–1114, Jul. 2018. DOI:10.1587/transfun.E101.A.1101

[32] H. Cember and T.E. Johnson, "Interaction of radiation with matter," in Introduction to Health Physics 4th ed. New York, USA: McGraw-Hill, p.180, 2009.

[33] R.V. Hogg and J.W. McKean, "Maximum likelihood Methods," in Introduction to mathematical statistics, 8th ed. Boston, USA: Peason, 2019.

[34] R. B. Manfrino, J.A. G. Ortega and R.V. Delgado,"Numerical Inequalities," in Inequalities, Germany: Birkhaäuser Verlag AG, ch.1, Theorem1.3.1, p.9, 2009.

[35] H. Hirayama, Y. Namito, and A. Bielajew, "The EGS5 code system, report 2005-8," High Energy Accelerator Research Organization, Tsukuba, Japan, 2009.

Naohiro Toda   received a doctor of engineering degree from the Graduate School of Toyohashi University of Technology in 1990. He became an Assistant Professor in Information Engineering at the same university. In 1992, he became a Lecturer in Electrical Engineering at Maizuru National College of Technology. In 1994, he became a Lecturer in Information Engineering at Toyohashi University of Technology. He also served as a Visiting Researcher at the University of Southern California in 1995. In 1999, he became an Associate Professor in the Department of Information Science and Technology of Aichi Prefectural University, and in 2002 he became a Professor. His research interests are medical imaging, signal processing, and nonlinear time series analysis. He is a full member of IEEE and Society of Instrument and Control Engineers.

Tetsuya Nakagami   received his master's degree in Information Science from the Graduate School of Aichi Prefectural University in 2017. He is currently working at DENSO CREATE INC. Technical Resources Department. His main research interest is theoretical analysis for estimating the attenuation coefficient of X-ray computed tomography.